Journal of
Materials Chemistry A

Accepted Manuscript

Volume 4 | Number 1 | 7 January 2016 | Pages 1–330

Journal of
Materials Chemistry A

Materials for energy and sustainability
www.rsc.org/MaterialsA

ISSN 2050-7488

ROYAL SOCIETY OF CHEMISTRY

PAPER
Kun Chang, Zhaorong Chang et al.
Bubble-template-assisted synthesis of hollow fullerene-like
MoS₂ nanocages as a lithium ion battery anode material

175 YEARS

This is an Accepted Manuscript, which has been through the Royal Society of Chemistry peer review process and has been accepted for publication.

Accepted Manuscripts are published online shortly after acceptance, before technical editing, formatting and proof reading. Using this free service, authors can make their results available to the community, in citable form, before we publish the edited article. We will replace this Accepted Manuscript with the edited and formatted Advance Article as soon as it is available.

You can find more information about Accepted Manuscripts in the author guidelines.

Please note that technical editing may introduce minor changes to the text and/or graphics, which may alter content. The journal's standard Terms & Conditions and the ethical guidelines, outlined in our author and reviewer resource centre, still apply. In no event shall the Royal Society of Chemistry be held responsible for any errors or omissions in this Accepted Manuscript or any consequences arising from the use of any information it contains.

ROYAL SOCIETY OF CHEMISTRY

rsc.li/materials-a

Table of contents
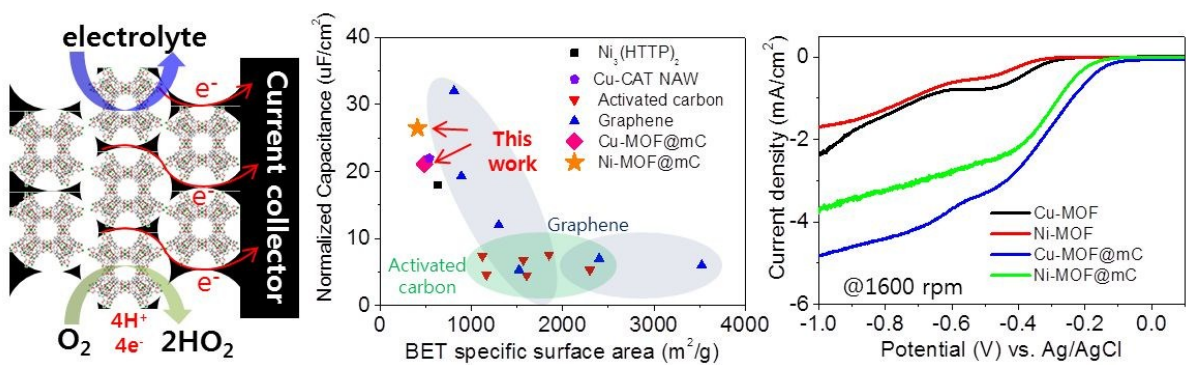
The electrochemical performance of MOFs for supercapacitor and oxygen reduction reaction is significantly improved when conjugated with conductive and 3D connected nanoporous carbon matrices.

Boost-up Electrochemical Performance of MOFs via Confined Synthesis within Nanoporous Carbon Matrices for Supercapacitor and Oxygen Reduction Reaction Applications

Hee Soo Kim[a], Min Seok Kang[a], and Won Cheol Yoo[a, b*]

[a]Department of Applied Chemistry, Hanyang University, 55 Hanyangdaehak-ro, Sangnok-gu, Ansan, Gyeonggi-do, 15588, Republic of Korea

[b]Department of Chemical and Molecular Engineering, Hanyang University, 55 Hanyangdaehak-ro, Sangnok-gu, Ansan, Gyeonggi-do, 15588, Republic of Korea

Corresponding Author[*]

e-mail: wcyoo@hanyang.ac.kr

1

Abstract

Utilizations of metal-organic frameworks (MOFs) for electrochemical applications are significantly limited by insulating nature and mechanical/chemical instability thereof. One promising approach for the deployment of conventional MOFs in electrochemical applications is to fabricate MOF-based hybrids (MBHs) with conductive materials, which facilitate effective electron transfer via conductive additives between MOFs. Herein, we present a facile method for effective filling of Cu- and Ni-HKUST-1 (Hong Kong University of Science and Technology, and denoted hereafter Cu-/Ni-MOF) inside 3D ordered mesoporous carbon (24 nm, mC), 3D ordered N-doped macroporous carbon (300 nm, NMC), and 3D ordered macroporous carbon (300 nm, MC), denoted as MOF@mC, MOF@NMC, and MOF@MC, respectively. The MOF@carbon matrix (MOF@CM) composites were intended for use as electrodes for electric double layer capacitors (EDLCs) and as electrocatalysts for the oxygen reduction reaction (ORR). EDLC performance of MOFs can be significantly improved by facilitating electron transfer through 3D conductive CM, reducing the electron pathway within insulating MOF using CM with small pores, and choice of metal center with pronounced faradaic nature. Ni-MOF@mC exhibited superior specific surface area normalized areal capacitance (26.5 $\mu F/cm^2$), exceeding most carbons and MOF-based EDLCs and outstanding long-term stability (91%@5000th). Furthermore, Cu-MOF@mC resulted in pronounced ORR activities, excellent methanol tolerance, and long-term stability. It is clearly demonstrated that conventional MOFs can be utilized for EDLC and ORR when conjugated with a 3D-connected nano-sized CM.

Journal of Materials Chemistry A Accepted Manuscript

Introduction

MOFs are crystalline porous materials composed of metal nodes and organic struts with high surface areas and versatile structural and compositional tunabilities[1]. Because of these fascinating properties, MOFs have been actively utilized for CO_2 capture and H_2 storage[2-3], heterogeneous catalysts[4-5], and chemical sensors[6]. However, the electrochemical applications of MOFs are severely hindered due to their almost insulating nature and mechanical/chemical instability[7-10].

Utilization of MOFs as electrodes for supercapacitors (SCs) is of considerable interest owing to their ultrahigh surface areas (up to 7000 m^2/g)[11] and structural flexibility, whose surface areas are much higher than those of carbonaceous materials that are mainly used as electrodes for SCs. SCs are electrochemical capacitors with high power densities and excellent cyclabilities; they are considered to be emerging electrical-energy storage materials[12-13]. Electrical energy can be stored either at the electrical double layer (EDL) of the electrode surface where electrolyte ions are adsorbed[12-18] or by redox reactions at the electrode surface[19-22]. For EDL capacitors (EDLCs), a high surface area and electrical conductivity are of utmost importance. Both properties, however, are not easy to achieve simultaneously; therefore, carbonaceous materials such as activated carbons, carbide-derived carbons, mesoporous carbons, carbon nanotubes (CNTs), and graphenes, which are known for their high surface areas and good electrical conductivities, have been actively employed as electrodes for EDLCs. In this regard, MOFs with exceptional porosities and tailor-made pore structures have emerged as a new class of electrode materials for high-performance EDLCs[12, 15-18, 23-28].

MOFs were initially used as precursors/templates for carbonaceous materials via thermolysis as electrodes for EDLCs[29-35]. After the Xu group reported MOF-5 derived carbon as electrodes of EDLCs[30], numerous papers were published[29, 31-36]; however, this approach does not harness the unique properties of MOFs[37-40]. In this context, one strategy is to synthesize a new type of MOF with high electric conductivity. Dinca and co-workers recently reported Ni_3 (2,3,6,7,10,11-hexaiminotriphenylene)$_2$ ($Ni_3(HITP)_2$) that exhibited a high electrical conductivity of 5000 S/m, which is comparable to that of graphite[41]. An EDLC was fabricated using conductive $Ni_3(HITP)_2$ without conductive additives and binders; it exhibited a superior specific surface area (SSA) normalized capacitance of 18 $\mu F/cm^2$ as compared to those of most carbonaceous materials, except for holey graphene. In addition, the mechanical stability of the

EDLC was improved by the compression of the MOF powder, resulting in a high volumetric capacitance. Li et al. reported that conductive Cu-MOF nanowire arrays (Cu-CAT NWAs) were synthesized directly on carbon fiber paper as electrodes for solid state SCs without conductive additives and binders[42]. Such Cu-CAT NWAs exhibited a high SSA normalized capacity of 22 $\mu F/cm^2$, good long-term cycle performance of 85% at 5000 cycles, and energy density of 2.6 Wh/kg with a powder density of 200 W/kg in the full-cell configuration. Although such synthetic approaches have opened up new avenues to employ MOFs directly as electrodes for EDLCs, the production costs and limitations in structural and compositional flexibility impose great challenges.

An alternative approach is to utilize conventional MOFs with conductive materials such as graphene and conductive polymers[43-48]. Yaghi and co-workers first reported MOF-based hybrids (MBHs) with graphene; 23 different nanocrystalline MOFs with several hundred nanometers in size were wrapped with 2D graphene sheets to fabricate electrodes for SCs. These electrodes were designed to minimize the diffusion of electrolyte ions into the MOFs and facilitate electric conductivity via graphene between the nano-sized MOFs. The authors examined the effect of various factors, including structure type, organic functionality, geometry and size of the secondary building unit, and pore size. They observed that a Zr-containing MOF (nMOF-867) exhibited superior areal and volume capacitances of 5.09 mF/cm^2 and 0.644 F/cm^3, respectively[46], and maximum energy and power densities of 0.00385 mWh/cm^2 and 8.67 mW/cm^2, respectively. In addition, Wang et al. reported ZIF-67 with several hundreds of nanometers in size interwoven with electrochemically deposited polyaniline (PANI) for flexible solid state SCs[47]. Conductive PANI indeed increased the electrical conductivity of the composite and enhanced faradaic processes across the interface. An areal capacitance of 35 mF/cm^2 and maximum energy and power densities of 0.0044 mWh/cm^2 and 0.245 W/cm^2, respectively, were achieved in a full-cell configuration.

To ensure the high-performance of MBHs for EDLCs, effective electron transfer between MOFs should be accomplished using conductive additives. It should be noted that the physical mixing of conductive materials and MOFs does not prevent the aggregation of insulating MOFs, which deteriorates the performance of the SCs[43]. In addition, it is better to minimize the electron transfer pathway length within the insulating MOFs; in other words, smaller MOFs may be better for shortening the electron transfer length and eventually, the

electrons are delivered to the current collector via the conductive materials. Unfortunately, there are very few reports on monodisperse MOFs (<100 nm) synthesized by conventional methods[49]. In this regard, the confined synthesis of MOFs inside the nanopores of carbonaceous materials may be a possible solution. The confined synthesis is of highly interests due to ability to mold the nanostructures dictated by a porous preform.[50-55] Pre-defined nanoporous architectures of carbonaceous materials can provide 3D-connected conductive networks that effectively deliver electrons from the MOFs to the current collector as well as reduce the size of MOFs within nanopores that substantially minimize the electron pathway within insulating MOFs. There are several reports on the successful synthesis of MOFs inside carbon nanofibers and macroporous carbons; however, the effective filling of MOFs inside nanoporous matrices by solvothermal methods is not readily achieved[56-59]. Recently, solid state synthesis of various MOFs inside mesoporous materials was reported; an effective filling of up to ca. 37 wt% was achieved[60].

On the other hand, the oxygen reduction reaction (ORR) is one of the most important reactions in fuel cells and metal-air batteries[61-67]. Pt-based electrocatalysts are mainly employed for ORR at the cathode; however, the high cost and poor long-term stability of Pt are major obstacles for expanding the use of Pt-based electrocatalysts[61, 63, 65]. MOFs with high surface areas and tunable chemical structures can be good candidates for non-Pt based ORR electrocatalysts. Recently, conductive $Ni_3(HITP)_2$ has been reported to show an ORR activity comparable with that of non-Pt based catalysts and good long-term stability[68]. In addition, Fe-porphyrin MOF and Cu-MOF with graphene oxides exhibited ORR activities and stable durabilities, indicating that the ORR activity of conventional MOFs increased upon functionalization with conductive additives[69-70].

To enhance the electrochemical performance of MBHs for EDLCs and ORR, it is necessary to coat the MOFs with nano-sized and 3D-connected conductive networks. Herein, we present a facile method for the effective filling of HKUST-1 (Cu and Ni) inside 3D ordered mesoporous (24 nm) and N-doped macroporous and macroporous (300 nm) carbons (Cu-/Ni-MOF@mC/NMC/MCs), which were utilized as electrodes for EDLCs and as electrocatalysts for ORR. An effective pore-filling of 57% of HKUST-1 was achieved throughout the CM when solid precursors placed inside the CM were transformed to MOFs through one time of solvent vapor-assisted crystallization (VAC) process.

5

Using the features of the VAC process, we examined the several important aspects including the effects of the conductive additive, conductivity (N-doping) and pore size (24 nm vs. 300 nm) of the CM, for the first time, and different metal centers of the MOFs, which significantly impact EDLC and ORR performance. Cu-MOF@MC exhibited a much higher EDLC performance (capacitance, rate retention, and long-term stability) than that of pristine MOF; furthermore, the performance of Cu-MOFs synthesized in a matrix of highly conductive carbon doped with nitrogen (Cu-MOF@NMC) was higher than that of Cu-MOF@MC. These results strongly imply that the electrochemical performance of MOFs can be significantly improved by facilitating electron transfer through 3D conductive carbon networks. In addition, Cu-MOF@mC exhibited a higher EDLC performance than that of Cu-MOF@MC/NMCs, suggesting that a reduced electron pathway length within the insulating MOF by using conductive additives of small pore sizes effectively increases the overall electric conductivity of the composite and improves the EDLC performance.

Furthermore, the effects of the metal center of MOFs were also studied. Ni-MOF@mC exhibited a higher EDLC performance than that of Cu-MOF@mC probably attributed to more pronounced redox nature of Ni center, with a high capacitance of 109 F/g, outstanding long-term stability of 91% at 5000 cycles, excellent SSA normalized capacitance of 26.5 $\mu F/cm^2$, exceeding those reported for the most carbons and MOF electrodes for EDLCs, and maximum energy and power densities of 38.8 Wh/kg and 21005 W/kg, respectively.

In addition to the excellent EDLC performance, Cu-MOF@mC exhibited a pronounced ORR activity, excellent methanol tolerance, and long-term stability, thus confirming that MOFs with large surface areas, well-defined pore structures, and chemical tunabilities can be employed as electrocatalysts for ORR when conjugated with 3D-connected and nano-sized conductive networks.

Experimental Section

6

Reagents and Chemicals

$Cu(NO_3)_2 \cdot 2.5H_2O$ (98%), oxalic acid (99%), KOH (90%), L-lysine (98%), polyvinylidene fluoride (PVDF), Nafion (5wt%), Super P, N-methyl-2-pyrrolidone (NMP), and dopamine hydrochloride (99%) were purchased from Sigma Aldrich. THF (tetrahydrofuran, 99%), 1,3,5-benzenetricarboxylic acid (H_3btc, 99%), HNO_3 (68%), $Ni(NO_3)_2 \cdot 6H_2O$ (98%), 2-methylimidazole (99%), and tetraethylammonium tetrafluoroborate ($TEABF_4$) were purchased from TCI. Resorcinol (98%) and furfuyl alcohol (99%) were purchased from Junsei. Tetraethylorthosilicate (TEOS, 98.0%), anhydrous ethanol (99%), dimethylformaldehyde (DMF, 99%), acetonitrile (MeCN, 99%), and sodium carbonate (98%) were purchased from Daejung.

Synthesis of Cu-MOF [$Cu_3(btc_2)$]

$Cu(NO_3)_2 \cdot 2.5H_2O$ (500.0 mg, 2.15 mmol) was dissolved in THF (6 mL) and H_3btc (300 mg, 1.43 mmol) was later added to this solution. To prevent the crystallization of Cu-MOF, 0.2 mL of HNO_3 was added to the mixture. After stirring for 10 min, the color of the solution became transparent. Later, pumps were used to draw out the solution over a period of 12 h. After 12 h, sky-colored dried powder was obtained. The dried materials were kept in a glass vial and reacted in a bomb reactor with 5 g of the DMF solution at 100, 120 and 150 °C for 24 h (the DMF solution should be separate from the glass container). After collecting blue crystals at the end of this reaction period, they were washed with DMF and solvent exchanged with MeCN for 1D. The product was heated to 80 °C under a static vacuum for 12 h.

Synthesis of MC and NMC

Initially, poly methyl methacrylate (PMMA) colloidal crystals were prepared using a previously reported emulsifier-free emulsion polymerization method[54]. They were then used as templates for the synthesis of MC and NMC. Subsequently, MC was prepared by the polymerization and carbonization of a resorcinol-formaldehyde (RF) sol catalyzed with sodium carbonate (molar ratio of resorcinol:formaldehyde:sodium carbonate = 1:2:0.019). The mixture sol was allowed to infiltrate the PMMA colloidal crystal template and cured at 90 °C for 1 d. Template removal and carbonization of the RF framework were achieved by heating the composite at 800 °C for 3 h in a nitrogen environment at a heating rate of 4.3 °C/min. Secondly,

to prepare N-doped MC (NMC), dopamine was employed. During the MC synthesis process, 0.6 g of dopamine was added to the RF sol precursor. The following procedure is the same as that used to synthesize MC. The resulting materials are denoted as MC and NMC, respectively.

Synthesis of mC

Before the synthesis of 24 nm mC, 40 nm SiO_2 nanoparticle arrays were prepared as templates. *fcc* packed silica nanoparticles were prepared using a previously reported method with some modifications[55]. Typically, L-lysine (0.15 g) was dissolved in 150 mL of deionized (DI) water and then stirred vigorously for 15 min to generate a homogeneous solution. Later, 20.8 g of tetraethyl orthosilicate (TEOS) was added to the solution and the mixture was stirred for 15 min. The resultant solution was transferred and completely sealed in a high-density polypropylene bottle and kept at 90 °C for 48 h. Subsequently, 20.8 g of additional TEOS was added to the solution. The silica particles were then placed in a convection oven heated to 85 °C to evaporate the solvent and the close-packed silica nanoparticles were calcined at 700 °C for 3 h under air to remove any remaining lysine. Later, mC was prepared by the polymerization and carbonization of a furfuyl alcohol mixture catalyzed with oxalic acid (molar ratio of furfuyl alcohol:oxalic acid = 183:1). The sol mixture was used to infiltrate a SiO_2 nanoparticle array template and cured at 90 °C for 1 d. Carbonization was carried out at 800 °C for 3 h in a nitrogen environment at a heating rate of 4.3 °C/min. To remove SiO_2 nanoparticles, the SiO_2/mC composite was placed in a 6 M KOH solution and stirred vigorously for 24 h, which repeated for 3 times at least. After removing the SiO_2 particles, the composite was washed with ethanol and water. The resulting material is denoted as mC.

Synthesis of Cu-MOF@MC, Cu-MOF@NMC, and Cu-MOF@mC

Firstly, the same condition of Cu-MOF precursor solution was prepared and 0.5 mL of Cu-MOF solution added into a glass vial containing the crushed 30 mg of MC and NMC and 40 mg of mC. Then vacuum drying process for removing THF solvent was applied and this process was repeated several times to fill the pore volume of CMs. The Cu-MOF precursor@CMs were kept in a glass vial and placed in a bomb reactor with 5 g of the DMF solution located peripherally at 120 °C for 24 h. To remove the MOFs on the surface of the CMs, vigorous sonication process was conducted for at least 10 min for several times. These

samples were denoted as Cu-MOF@MC, Cu-MOF@NMC, and Cu-MOF@mC, respectively.

Synthesis of Ni-MOF [Ni$_3$(btc)$_2$]

Ni(NO$_3$)$_2$·6H$_2$O (2.28 g, 7.8 mmol) was dissolved in DMF (15 mL), 0.2 mL HNO$_3$, and H$_3$btc (1.23 g, 5.85 mmol); 2-methylimidazole (0.33 g, 4.02 mmol) was later added to this solution. After stirring for 30 min, 3 mL of this solution was transferred to a Teflon-liner. Reaction was allowed to occur at 170 °C for 48 h, after which the reactor was allowed to cool down to the room temperature. Greenish crystals were collected as the reaction product. After washing with DMF and solvent exchange with MeCN for 1 d, the product was dried at 90 °C under static vacuum for 12 h.

Synthesis of Ni-MOF@mC

The Ni-MOF precursor solution (2 mL) was added into a Teflon-liner containing 40 mg of mC, which was underwent 170 °C for 48 h and whole process was repeated for three times for effective filling MOF inside mC. To remove the MOFs on the carbon surface, vigorous sonication process was conducted for at least 10 min for several times. The resultant sample was denoted as Ni-MOF@mC.

Electrochemical measurements on a two-electrode system (symmetric cell)

All the electrodes were prepared by mixing the active materials (80 wt%), Super P (10 wt%), and PVDF (10 wt%) with NMP as a solvent to form slurries, which were then pasted onto the carbon paper (Sigracet 29AA) using a doctor blade to achieve a thickness of 30 μm. The electrode was dried overnight under vacuum oven at 80 °C. The symmetric SCs were fabricated using two pieces of electrodes with TEABF$_4$ (1 M) in MeCN as an electrolyte and TP20 membrane (Wellcos Corporation) as a separator, which were assembled in coin cell (CR2032) container. All the tests were performed at room temperature. Gavanostatic charge-discharge, Cyclic voltammetry (CV), and long-term stability analyses were performed on a CHI660E instrument, and the charge-discharge curves and CV profiles were recorded from 0 to 3.2 V. Gravimetric capacitance C (F/g) was calculated according to the following equation using the discharge portion of the charge-discharge curves:

$$C = \frac{2(I \Delta t)}{m \Delta V}$$

where I, Δt, m, and ΔV are the applied current, discharge time, the mass of one electrode active material, and maximum voltage change, respectively. Energy density (E) and power density (P) are calculated according to the following equation:

$$E = 0.125 \times C \Delta V^2 \quad , P = \frac{E}{\Delta t}$$

RDE measurements

The catalyst ink was prepared by mixing catalyst samples (10 mg) with 0.7 ml of MeCN (including 60 μL of 5wt% Nafion) solution. This catalyst ink was deposited on a glassy carbon electrode (0.15 cm in diameter) in a rotating disk electrode (RDE) and dried at room temperature. The catalyst loading was 0.12 mg/cm^2. All electrochemical measurements were conducted in a conventional three-electrode cell with platinum wire, saturated Ag/AgCl reference, and the catalyst-coated RDE electrode, which was controlled on a CHI660E instrument. The electrolyte was 0.1 M KOH solutions. CV was performed in the potential range of 0.1 to - 1.0 V (vs. Ag/AgCl) with a scan rate of 50 mV/s under N_2-/O_2-saturated 0.1 M KOH solution. RDE polarization curves were conducted in O_2-saturated 0.1 M KOH at 400 to 1600 rpm (400 to 3500 rpm for Cu-/Ni-MOF@mCs) with scan rate of 5 mV/sec. The electron transfer number and the kinetic current density were estimated by following Koutecky-Levich (KL) equation with using the RDE data at 400, 900, 1200, 1600 rpm.

$$\frac{1}{i} = \frac{1}{i_L} + \frac{1}{i_K} = \frac{1}{B\omega^{1/2}} + \frac{1}{i_K}$$

$$B = 0.62nFC_0(D_{O_2})^{2/3}v^{-1/6}$$

Here, i, i_L and i_K are the measured, diffusion limiting and kinetic current density,

respectively. ω is the rotating speed of electrode, F is the Faraday constant (98485 C/mol). C_0 is the saturated O_2 concentration in bulk solution (0.1 M KOH: 1.21 x 10^{-6} mol/cm), D_{O_2} is the diffusion coefficient of O_2 (0.1 M KOH: 1.86×10^{-5} cm^2/s), and υ is the kinetic viscosity of electrolyte (0.01 cm^2/sec). The methanol tolerance test was conducted with chronoamperometry at a constant voltage of -0.4 V vs. Ag/AgCl with rotating at 1600 rpm. 1M methanol was added to electrolyte at 500 s. The long-term stability was conducted on 2000 cycles of potential cycling between 0 V to -0.4 V vs Ag/AgCl at sweep rate of 50 mV/s in O_2-saturated 0.1 M KOH solution.

Characterization

Low-temperature nitrogen sorption isotherms were measured at 77 K on an adsorption volumetric analyzer (BEL Mini, BEL Inc., Japan). The samples were degassed at 90 °C for 12 h under static vacuum before adsorption measurements. The specific surface area was determined using the BET method from the nitrogen adsorption isotherms in the relative pressure range of 0.05 to 0.20. The pore size distributions were obtained from the corresponding adsorption branches using the BJH method. The micropore volumes were calculated using the *t*-plot method. SEM images were obtained on a HITACHI S-4800 microscope operating at an accelerating voltage of 15.0 kV. Elemental analysis (EA) was conducted on a FLASH EA1112 instrument and TEM images were recorded on a JEM-3100F instrument. High-angle annular dark-field scanning transmission electron microscopy (HAADF-STEM) was utilized for elementary mapping of the specimen. TGA results were obtained using a SDT Q600 device (TA Instruments Inc.). XRD patterns were generated on a Rigaku D/MAX-2500/PC instrument using Cu Kα radiation (λ = 1.5406 Å). Electrochemical impedance spectroscopy (EIS) measurements were made using CHI 660H potentiostat between 0.01 Hz to 10 kHz at 5mV amplitude voltage.

Results and discussion

Synthesis of MOF@CM

For the electrochemical applications of high-performance MBHs, effective electron

11

transfer via conductive additives between MOFs should be accomplished without the physical aggregation of MOFs. In this regard, 3D ordered and connected mC and MC are suitable as conductive materials bearing MOFs. Electron transfer can be facilitated through a 3D carbon framework and mass diffusion can also be expedited through the windows where the pores are connected. In addition, the CM should be chemically stable for the solvothermal reaction to occur and it should be inert for MOF growth inside it. Thus, we prepared 3D ordered and connected carbon frameworks using a hard templating method. Colloidal crystals composed of monodisperse PMMA spheres of ca. 400 nm were used as the hard template (Figure S1a); it was infiltrated by either a resorcinol-formaldehyde (RF) sol or a RF sol with a dopamine additive as the nitrogen source to produce MC and NMC, respectively. During carbonization, PMMA spheres were thermally decomposed, resulting in MC and NMC; the nitrogen content of the latter was determined by elementary analysis to be 2.3%. According to SEM images (Figure S1b and c), macropores around 300 nm with a smooth surface were arranged in an inverse *fcc* configuration in both carbons; they were connected via 12 windows where PMMA spheres were originally connected with each other. In addition, monodisperse silica spheres of around 40 nm were synthesized using lysine as the base catalyst and surfactant. It also served as a cross-packing agent via hydrogen bonding during the drying process, resulting in highly ordered 3D colloidal crystals as reported elsewhere (Figure S1d)[55]. The silica colloidal template was infiltrated by furfural alcohol, which was polymerized, and subsequently carbonized. After etching the silica template by KOH, mC was successfully prepared. As revealed by SEM observations (Figure S1e), the highly ordered and hollow structure of mC indicates a perfect replication of the colloidal crystal template. TEM image and the corresponding Fourier pattern also implied that the highly ordered mesopores of mC were successfully transferred from the silica colloidal template (Figure S1f).

To effectively fill Cu-MOF inside the CM, VAC was conducted. The metal and ligand precursors were first dissolved in THF and HNO_3 was added to prevent the formation of a nonporous coordination polymer[71], which was readily formed without HNO_3. The clear precursor solution was then infiltrated into the CM and vacuum drying was conducted at room temperature to remove the solvent, resulting in a solid mixture of precursors inside the CM (precursor@CM). This incipient wetness impregnation process was repeated until the entire pore volume of the CM was filled up. Precursor@CM was placed in the glass vial, which was

then placed at the bottom of a Teflon-liner where DMF was located peripherally. It was then crystallized using the solvent vapor at elevated temperatures of 120 °C for 24 h, as illustrated in scheme 1.

In order to confirm the synthesis condition, Cu-MOF was firstly synthesized by VAC without CM at 100, 120, and 150 °C for 24 h. According to the XRD results, three Cu-MOFs exhibited well-developed peaks corresponding to the simulated HKUST-1 (Figure S2a). N_2 sorption measurements revealed that the Cu-MOF synthesized at 120 °C for 24 h showed a higher microporosity of 0.49 cc/g when compared to those (0.35 and 0.23 cc/g) of Cu-MOF prepared at 100 and 150 °C, respectively. (Figure S2b and Table 1). Therefore, the synthesis condition for Cu-MOF was optimized at 120 °C for 24 h. The SEM image of Cu-MOF indicated a regular morphology similar to that of a truncated octahedron; its size was in the range of several microns (Figure S2c). Later, Cu-MOF@MC was prepared by VAC at 120 °C in 24 h. With respect to the 1st round of VAC (Cu-MOF@MC-1), low-magnification SEM revealed that a relatively large area of MC was filled with particles (Figure 1a). High-magnification SEM images showed that some of the macropores were filled with smooth particles; on the other hand, some of the particles exhibited sharp edges and small buds were also observed within the windows, which are highlighted by red circles in Figure 1b. After the 2nd round of VAC (Cu-MOF@MC-2), nearly all the macropores of MC were filled with particles resembling PMMA spheres, which were used as the hard template (Figure 1c and d). It seems that the shape development of MOF inside the macropores of MC initially started with a characteristic morphology and was then limited by the confined space of macropores, resulting in particles with smooth surfaces. Similar growth patterns were reported on the confined synthesis of zeolites inside nanoporous CM[54,72].

In the XRD patterns, characteristic peaks corresponding to HKUST-1 were identified for Cu-MOF@MC-1, confirming that Cu-MOF was successfully synthesized inside MC by VAC (Figure 1e). After the 2nd round of VAC, much intense XRD peaks were observed. Sequential VAC processes allowed more Cu-MOF growth inside MC. N_2 sorption analysis was also performed. The abrupt increase in N_2 uptake in Cu-MOF@MC-1 when compared to that of MC at very low relative pressures was attributed to the microporosity of MOF synthesized inside MC; the porosity was higher in Cu-MOF@MC-2 (Figure 1f). The micropore volumes were determined by the t-method and the total pore volumes obtained at 0.99 P/P_0 of Cu-

13

MOF@MC-1 and 2 were 0.28 and 0.33 cc/g and 0.42 and 0.44 cc/g, respectively, while their BET surface areas were 743 and 848 m^2/g, respectively. These values are much higher than those of MC (0.15 cc/g, 0.25 cc/g, and 391 m^2/g) (Table 1). In addition, TGA was conducted for Cu-MOF@MC-2 in an air atmosphere. A CuO content of 25.7 wt% could be confirmed (Figure 1g and Figure S3). Combining the N_2 sorption and TGA results, the pore-filling of Cu-MOF inside MC after the 1st round of VAC was calculated as volume fractions of MOF with 64 and 57% determined by micropore volume and TGA value, respectively (Table 1 and Note 1 in the supporting information for the detail calculation). Furthermore, volume fractions of Cu-MOF for Cu-MOF@MC-2 (denoted Cu-MOF@MC hereafter) were reached up to 76 and 78% determined by micropore volume and TGA value, respectively (Table 1). Meanwhile, Cu-MOF@MC underwent thermolysis in a N_2 atmosphere (800 °C) that Cu nanoparticles less than 100 nm were spatially placed throughout the macropores of MC confirmed by XRD and SEM measurements, strongly indicating that synthesized Cu-MOF was well distributed within MC (Figure S4a and b). Such effective pore-filling with more than half of the free volume of CM by only one VAC process has rarely been accomplished for conventional solvothermal reactions, which previously limited the expansion of MOF@CM for electrochemical applications.

In order to investigate the effect of the conductivity of the CM on the electrochemical performance of MBHs, Cu-MOF was prepared via a sequential VAC process inside N-MC. From the SEM images (Figure S5a and b), it can be inferred that almost all the macropores of NMC were filled with smooth particles after the 2nd round of VAC, clearly confirming the successful synthesis of Cu-MOF@NMC. XRD analysis identified characteristic peaks corresponding to HKUST-1, which were generated from Cu-MOF inside CM (Figure S5c). N_2 sorption measurements also confirmed that Cu-MOF@NMC exhibited a high uptake at very low relative pressures, due to the formation of a MOF inside the macropores (Figure S5d). The micropore and total pore volumes and BET surface area of Cu-MOF@NMC were 0.32 cc/g, 0.41 cc/g, and 808 m^2/g, respectively. These values are much higher than those of NMC (0.11 cc/g, 0.18 cc/g, and 302 m^2/g, respectively). A similar trend was observed for Cu-MOF@MC as well (Table 1). The TGA data indicated a leftover residue of 24.7 wt% (Figure S5e). The volume fractions of MOF inside NMC determined by N_2 sorption measurement and TGA result, respectively, were both 75% (Table 1).

Furthermore, Cu-MOF was synthesized inside the mesopores of mC via a sequential VAC process. After the 3rd round of VAC (Cu-MOF@mC), nearly all the mesopores were clogged with unshaped matter, which was not visible in SEM images; these observations are compared to that of the mC template (Figure 2a and Figure S1e). TEM analysis revealed that ordered mesopores could no longer be observed and part of mC indicted in the Figure 2b was much darker than the other areas. This region is definitively different from the mC template (Figure S1f). Crystalline micropores of Cu-MOF were not clearly observed under TEM investigation probably due to vulnerable nature of micropores of MOF under TEM investigation (Figure 2b inset). Further elementary mapping of Cu-MOF@mC was conducted along with high-angle annular dark field image in scanning transmission electron microscope (HAADF-STEM) analysis; the presence of C, Cu, and O elements in the specimen could be attributed to the CM, Cu metal center, and oxygen moiety of the ligand of Cu-MOF, respectively (Figure 2c–f). XRD analysis of this sample showed signature reflections of HKUST-1, clearly confirming the successful preparation of Cu-MOF inside the mesopores of mC (Figure 2g). N_2 sorption isotherms of Cu-MOF@mC indicated a higher uptake at a very low relative pressure and a reduced uptake for hysteresis when compared to those of mC (Figure 2h). These observations could be ascribed to the formation of micropores of MOF and blockage of mesopores of mC, respectively. The BJH pore size distribution centered ca. 24 nm for mC was significantly reduced due to the Cu-MOF synthesized inside mC (inset in Figure 2h; hereafter the pore size of mC is defined as 24 nm). A significantly augmented micropore volume of 0.28 cc/g was obtained for Cu-MOF@mC compared to that of mC (0.04 cc/g); in contrast, a huge decrease was observed in the total pore volume (0.92 cc/g) and surface area (488 m^2/g), when compared to those of mC (4.0 cc/g and 1107 m^2/g, respectively) (Table 1). The former should be ascribed to the microporosity developed due to MOF synthesis inside mC and the latter issue can probably be attributed to the pore-blockage of the mesopores of mC. TGA results indicated a leftover residue of 22.7 wt.% (Figure 2i). The volume fractions of MOF inside mC were of 68% and 69% determined by micropore volume and TGA data, respectively (Table 1 and Note 1). These results support the effective pore-filling of MOF inside the mesopores of mC by VAC.

In order to investigate the effect of the metal center of MOF for EDLC and ORR applications, we attempted to synthesize Ni-MOF via VAC; unfortunately, Ni-MOF could not

be successfully synthesized by VAC, probably due to the less reactive nature of Ni ions for crystal formation[73]. Thus, highly concentrated metal and ligand precursor solutions in DMF with HNO_3 and a 2-methylimidazole modulator was employed for the solvothermal reaction at 170 °C for 48 h (see the experimental section for more information). According to the XRD results, the peaks of as-prepared Ni-MOF are well matched with the characteristics of HKUST-1 (Figure S6a) and the N_2 sorption isotherm showed a type I behavior representing microporosity (Figure S6b) with the surface area of 561 m^2/g (Table 1). The SEM image indicated less regular crystals with smooth surfaces and their size was in the range of 5 to 10 μm (Figure S6c). In the case of Ni-MOF@mC, Ni-MOF was synthesized in mC via a conventional solvothermal reaction. mC was soaked in a highly concentrated precursor solution, which then underwent three solvothermal reactions for the effective filling of MOF inside mesopores. According to the SEM figures (Figure S7a), almost all mesopores of mC were filled with unshaped matter, as also observed by TEM analysis (Figure S7b). The XRD data of Ni-MOF@mC confirmed that Ni-MOF was synthesized inside mC (Figure S7c). The N_2 sorption measurement revealed an increased microporosity (0.17 cc/g) and decreased pore volume (0.55 cc/g) at a large relative pressure, which further confirmed the confined synthesis of Ni-MOF inside mC (Figure S7d). Combining the N_2 sorption and TGA data (18.5 wt%, Figure S7e), the volume fractions of Ni-MOF inside mC were as 67% and 59%, obtained from micropore volume and TGA result, respectively (Table 1 and Note 1).

Supercapacitor performance

The SC performance of Cu-/Ni-MOF, CM, and MOF@CMs was tested using a symmetric two-electrode full-cell configuration with a tetraethylammonium tetrafluoroborate ($TEABF_4$) electrolyte in an acetonitrile solution. CV of Cu-/Ni-MOF was carried out and reversible cyclic voltammograms were identified for both samples (Figure S8a and b). At faster scan rates, increased current densities with a relatively rectangular shape were observed, which indicated a capacitive nature for both samples in the working potential window range of 0 to 3.2 V (Figure S8a and b). There was no obvious faradaic process for Cu-MOF; on the other hand, a wide shoulder was observed around 1.8 V for Ni-MOF probably derived from the open Ni site, which might be attributed to the greater redox nature of Ni compared to Cu center (Figure S8a and b)[46,74-75]. Galvanostatic charge-discharge profiles of the pristine MOFs were

measured in the current density range of 0.3 to 50 A/g by chronopotentiometry (Figure S8c and d); the profiles of both samples showed IR drops. Such IR drops have been also reported for various MOFs with the same electrolyte solution and carbon spheres with pores smaller than 1 nm showed similar IR drop in the charge-discharge profile in a H_2SO_4 electrolyte solution[23,46]. The specific gravimetric capacitances of both MOFs were then obtained from charge-discharge profiles at various current densities (Table S1). Ni-MOF exhibited higher capacitances than Cu-MOF at all current densities. When considering the BET surface areas of Cu-/Ni-MOF, 1095 and 561 m^2/g, respectively (Table 1), the better performance of Ni-MOF could be attributed to the faradaic process of Ni center as identified by the CV profile (Figure S8b).

In order to analyze the enhancement in the electrochemical performance of MOF@CM, the SC performances of CM were first identified. The CV profiles of 3DOM/N-M/mCs exhibited capacitive behaviors with characteristic rectangular shapes (Figure S9a-c). The gravimetric capacitances of M/NM/mCs were calculated using charge-discharge profiles (Table S1). The highest capacitance was recorded for mC owing to its much larger surface area compared to those of other samples (Table 1). In contrast, the capacitances of NMC at all current densities were higher than those of MC, even possessed smaller surface area, probably attributed to N-doping that enhanced electric conductivity of CM. In order to analyze the effect of N-doping on conductivity gain, we performed electrochemical impedance spectroscopy (EIS) measurements. Nyquist plots were obtained and fitted into the equivalent circuit (Figure S10). An equivalent series resistance (R_e), which is the total resistance of the electrode materials, electrolyte, current collector, and full-cell case, and a charge transfer resistance (R_{ct}) were represented by semicircles in the high and medium frequency range for NMC and MC samples, those of which were 8.2 and 9.8 Ω for R_e and 2.9 and 3.1 Ω for R_{ct} values, respectively (Table S2)[25,76]. The smaller R_e and R_{ct} values of NMC should be attributed to the N-doping (2.3%), which enhanced the conductivity. In addition, mC presented smaller R_e (7.6 Ω) and R_{ct} (2.47 Ω) as compared to those of MC and NMC (Figure S10 and Table S2). The R_e is related to intrinsic conductivity of electrode and the R_{ct} is strongly related to the SSA and intrinsic conductivity of electrode; thus smaller R_e and R_{ct} of mC could possibly be attributed to different intrinsic conductivity derived from different precursor (furfuryl alcohol) used for mC and higher SSA (1107 m^2/g) as compared to those of MC (391 m^2/g) and NMC (302 m^2/g), respectively (Table 1).

We later measured the SC performance of MOF@CM samples. CV measurements indicated increased current densities with characteristic rectangular shapes at faster scan rates for all the composites (Figure S11a–d). The CV profiles of MOF@CMs and the pristine MOFs measured at a scan rate of 200 mV/s were compared; much higher current densities observed for MOF@CMs compared to those of the pristine MOF samples, clearly indicated a highly enhanced electrochemical performance (Figure 3a). In addition, the galvanostatic charge-discharge profiles of the composites were constructed at various current densities of 0.3 to 50 A/g (Figure S11e–h). The charge-discharge profiles at 0.5 A/g of a series of comparison groups such as Cu-MOF/MC/Cu-MOF@MC, Cu-MOF/NMC/Cu-MOF@NMC, Cu-MOF/mC/Cu-MOF@mC, and Ni-MOF/mC/Ni-MOF@mC was plotted. The MOF@CM composites exhibited much higher discharge times than those of the pristine MOFs and higher discharge times than those of the corresponding CMs as well (Figure S12a–d). The charge-discharge profiles at 0.5 A/g of the pristine MOFs and MOF@CMs are plotted in Figure 3b in order to clearly present the electrochemical enhancement of MOF@CMs. In addition, the gravimetric capacitances of the pristine MOFs, CMs, and MOF@CMs were obtained from the discharge times at various current densities and capacitance retentions at 50 A/g compared to the values obtained at 1 A/g. The MOF@CM composites exhibited much higher capacitances than the corresponding the pristine MOFs and CMs, and significantly enhanced retentions compared to MOF (Figure 3c, Figure 12e and Table S1). For instance, the capacitances of Cu-/Ni-MOF, MC/NMC/mC, Cu-MOF@MC/NMC/mC, and Ni-MOF@mC at 0.3 A/g were 8, 10, 25, 37, 73, 77, 95, 103, and 109, respectively (Figure 3c and Table S1). The capacitance of Cu-MOF@NMC was found to be ca. 23% higher than that of Cu-MOF@MC. Considering the similarities in pore size, surface area, and MOF content, the conductivity of CM seems to be crucial for good electrochemical performance. According to EIS measurements, the R_e and R_{ct} values of Cu-MOF@NMC were 6.02 and 1.4 Ω, respectively, which are smaller than those (7.7 and 2.1 Ω) of Cu-MOF@MC (Figure 3d and Table S2). Therefore, it can be presumably concluded that a high conductivity of CM is pivotal for efficiently enhancing the electrochemical performance of MOF@CM by facilitating electron transfer through 3D connected conductive CM.

In addition, Cu-MOF@mC exhibited a superior performance when compared to those of Cu-MOF@M/NMCs (Figure 3c and Table S1). The much smaller pore size of mC (24 nm)

when compared to that of MC/NMC (300 nm) could effectively reduce the electron pathway inside insulating MOF, resulting in an increase in overall electric conductivity of the composite. This hypothesis was also supported by EIS measurements; the R_e and R_{ct} values of Cu-MOF@mC were 3.8 and 0.9 Ω, respectively, which were much smaller than those of Cu-MOF@M/NMC (Figure 3d and Table S2). Furthermore, Ni-MOF@mC exhibited a higher capacitance of 109 F/g at 0.3 A/g than 103 F/g of Cu-MOF@mC at 0.3 A/g (Figure 3c and Table S1). When considering smaller MOF content (59 wt% determined by TGA) and surface area (411 m^2/g) of Ni-MOF@mC compared to those (69 wt% and 488 m^2/g) of Cu-MOF@mC, the higher capacitance for Ni-MOF@mC could be probably attributed to the redox ability of the Ni center as observed in the CV curve (Table 1 and Figure S8b). Meanwhile, the lower R_e (3.73 Ω) and R_{ct} (0.82 Ω) values of Ni-MOF@mC than those of Cu-MOF@mC (Figure 3d and Table S2) also supports the higher capacitance of Ni-MOF@mC.

To verify capacity enhancement (CE) of the MOFs by the 3D conductive CM, the CE values were calculated using the capacitances of the pristine MOFs and normalized capacitances (NCs) of MOFs, which were boosted by incorporation in a conductive CM. The weight contents of MOFs inside the CMs and the capacitances of MOF@CMs were employed for obtaining the NCs (Table S1 and Note 2 in the supporting information for the detail calculation). Figure 3e shows that the CE values of all the MOF@CM samples increased with an increase in the current density. It seems reasonable that the electrochemical response can be efficiently enhanced by the conductive CM with an increase in the current density because the insulating MOF cannot be effectively operated under fast electrolyte adsorption-desorption conditions. In addition, when the same Cu-MOF was prepared with different CMs, higher CEs were clearly identified in the order of Cu-MOF@mC > Cu-MOF@NMC > Cu-MOF@MC (Figure 3e); a similar trend was observed in the capacitances of these MOF@CM specimens. This could be due to the higher conductivity of the CM of Cu-MOF@NMC, which facilitates effective electron transfer, and a short electron transfer pathway in the insulating MOF of Cu-MOF@mC, resulting in a CE of 89 times achieved at 50 A/g (Figure 3e and Table S1). Furthermore, Ni-MOF@mC exhibited a CE of around 76 at 50 A/g due to its short electron transfer pathway and its faradaic characteristics (inset in the Figure 3e).

Meanwhile, the long-term stability of the samples was monitored at 5 A/g for 5000 cycles. Outstanding cyclabilities were identified for MOF@CMs when compared to those of

the pristine MOFs; Cu-/Ni-MOF@mC samples exhibited a superior stability of 91% (Figure 3f). Both Cu-/Ni-MOF@mC samples after 5000 cycles were analyzed by XRD measurements that characteristic HKUST-1 peaks were clearly identified (Figure S13a and b), strongly confirming the structural stability of the composites. According to SEM images, mesopores of mC of both samples were well preserved intact, surfaces of which were still covered with amorphous matter (Figure S13c and d). TEM images also revealed relatively well preserved mesopores with darker areas (Figure S13e and f), resembling to those before the long term stability test (Figure 2 and Figure S7).

Subsequently, we calculated the SSA normalized capacitances of the pristine MOFs and MOF@CMs. As expected, the pristine MOFs exhibited inferior capacitances of 0.7 and 1.8 $\mu F/cm^2$ at 0.3 A/g, respectively (Table S3 and Figure S14). On the other hand, Cu-MOF@M/NMCs exhibited capacitances of 9.1 and 11.8 $\mu F/cm^2$, respectively, while Cu-/Ni-MOF@mCs showed much higher areal capacitances of 21.1 and 26.5 $\mu F/cm^2$, respectively (Figure 4a, Figure S14, and Table S3). In particular, the SSA normalized capacitance of Ni-MOF@mC at 50 A/g still remained high at 12.7 $\mu F/cm^2$ (Table S3), which is strongly indicative of the effective utilization of the electrochemical surface area even at a high current density. It should be noted that the value of 26.5 $\mu F/cm^2$ obsersved for Ni-MOF@mC exceeds those of most carbonaceous materials except holey graphene and recently reported $Ni_3(HITP)_2$ (18 $\mu F/cm^2$) and Cu-CAT NWA (22 $\mu F/cm^2$) (Figure 4a and Table S4). In addition, Ni-MOF@mC exhibited maximum energy and power densities of 38.8 Wh/kg (0.042 mWh/cm^2) and 21005 W/kg (23 mW/cm^2), respectively (Figure 4b and Table S3 and S5). These values are superior and/or comparable to the values obtained from MOF-based EDLCs, as listed in Table S5.

ORR performance

The ORR activities of mC, pristine MOFs, and Cu-/Ni-MOF@mC samples were investigated using CV analysis in N_2-/O_2-saturated 0.1 M KOH solutions. The voltammograms of mC in N_2-/O_2-saturated electrolyte solutions exhibited a capacitive behavior, confirming the absence of significant ORR activity (Figure S15). When the CVs of the pristine MOFs were recorded in N_2-/O_2-saturated electrolyte solutions, the development of current density in the scanning range was very limited, probably due to the insulating nature of the MOFs (Figure S16). Meanwhile, the voltammograms of Cu-/Ni-MOF@mC samples measured in N_2-saturated

electrolyte solutions showed EDL capacity currents; on the other hand, notable development of cathodic current was observed for Ni-MOF@mC and in particular well-developed cathodic current was clearly identified for Cu-MOF@mC around –0.3 V (vs. Ag/AgCl) in an O_2-saturated electrolyte solution, indicative of the ORR activities of MOF@mCs (Figure S16).

To further investigate the ORR kinetics, RDE measurements were conducted in O_2-saturated 0.1 M KOH solutions (Figure S17). The polarization curves of the pristine MOFs showed negligible ORR activities; in contrast, the onset and half-wave potentials of Cu-/Ni-MOF@mC were shifted to a positive direction, –0.091 and –0.36 V (vs. Ag/AgCl) and –0.101 and –0.38 V (vs. Ag/AgCl), respectively (Figure 5a and Table S6), which is a clear indication of prominent ORR activity. More positive onset and half-wave potentials were identified for Cu-MOF@mC, probably due to the pronounced ORR activity of the Cu center[70,77], which were listed and compared with ORR activities obtained from MOF-based electrocatalysts in the Table S6. In addition, the Koutecky-Levich (KL) plots were obtained using polarization curves at various rotating rates (400–1600 rpm) of the disk electrodes in the voltage range of $−1.0$ to $−0.4$ V (vs. Ag/AgCl) (insets in Figure S17). The linearity and parallelism of the plots of the pristine MOFs were very poor; in contrast, a good linearity and parallelism was clearly observed for the MOF@CM samples, suggesting first-order reaction kinetics with respect to the dissolved O_2 molecule[66, 78-79]. The electron transfer number (n) per O_2 at various potentials ($−1.0$ to $−0.4$ V vs. Ag/AgCl) for the samples were calculated from the KL plots. Very poor n values were observed for the pristine MOFs at different potentials (Figure 5b). In contrast, much enhanced n values at various potential ranges were obtained for MOF@CM samples. In particular, Cu-MOF@mC exhibited higher n values over various potential ranges compared to those of Ni-MOF@mC, one of which reached up to 3.78 at –0.6 V (vs. Ag/AgCl) (Figure 5b). Furthermore, the kinetic current densities (j_K) of the samples at different potentials ($−1.0$ to $−$ 0.4 V vs. Ag/AgCl) obtained from KL plots are illustrated in Figure 5c; the pristine MOFs exhibited inferior j_K values at all potentials and MOF@CM samples exhibited higher j_K values than pristine MOFs. Further, Cu-MOF@mC exhibited higher j_K values than Ni-MOF@mC at all potentials, strongly indicating the pronounced ORR activity of the Cu center. The ORR activities of Cu-MOF@mC could be comparable with MOF-based electrocatalysts listed in the Table S6.

Finally, methanol tolerance and long-term stability tests were conducted for verifying

the robustness of the MOF@mC samples. A significant methanol oxidation current was observed for commercial Pt/C; in contrast, no response was observed for the Cu-/Ni-MOF@mC samples (Figure 5d), clearly confirming their tolerance to methanol crossover, which could be further applicable to direct methanol fuel cell under alkaline condition. In addition, negligible performance decays were observed after 2000 cycles for the MOF@mC samples, clearly confirming their long-term stability (Figure S18).

Conclusion

Conventional HKUST-1 (Cu & Ni) have been successfully and effectively synthesized inside various CMs using a VAC process. The different pore sizes (24 vs. 300 nm) and conductivities (MC vs. NMC) were utilized as conductive additives. All of the MOF@CM samples exhibited high EDLC performances, clearly confirming an enhancement in the electrochemical performance of MOFs with conductive additives. The order of electrochemical performances of MOF@CM samples is as follows: Cu-MOF@MC < Cu-MOF@NMC < Cu-MOF@mC < Ni-MOF@mC. The electrochemical performance of a MOF can be significantly improved by readily facilitating electron transfer through a more conductive CM (Cu-MOF@NMC > Cu-MOF@MC), by reducing the electron pathway length within the insulating MOF by using CM with small pores (Cu-MOF@mC > Cu-MOF@NMC/MC), and by choice of metal center with more pronounced faradaic nature (Ni-MOF@mC > Cu-MOF@mC). Therefore Ni-MOF@mC exhibited superior performances such as a high capacitance of 109 F/g, excellent SSA normalized capacitance of 26.5 $\mu F/cm^2$, exceeding most carbons and MOF-based electrodes for EDLCs, outstanding long-term stability of 91% at 5000 cycles, and maximum energy and power densities of 38.8 Wh/kg and 21005 W/kg, respectively.

In addition to excellent EDLC properties, MOF@mC samples exhibited superior ORR activities to the pristine MOFs presenting inferior ORR performances, among which Cu-MOF@mC showed pronounced ORR activities, excellent methanol tolerance, and long-term stability, comparable with non-Pt based electrocatalysts for ORR. Therefore, it can be confirmed that MOFs with high surface areas, well-defined pore structures, and chemical tunabilities can be utilized as electrodes for EDLCs and electrocatalysts for ORR when functionalized with 3D-connected nano-sized conductive networks, which could further be applicable to other types of electrochemical applications such as sensors and etc.

Supporting information

Additional SEM, TEM images, XRD, N_2 sorption isotherms, TGA results, CV profiles, charge-discharge profiles, Nyquist plots, polarization curves, KL plots, Tables, and Notes for detail calculations are included.

Author information

Corresponding Authors

* Tel.: +82-31-400-5504, E-mail: wcyoo@hanyang.ac.kr

References

1. H. Furukawa, K. E. Cordova, M. O'Keeffe and O. M. Yaghi, *Science,* 2013, **341**, 1230444.

2. K. Sumida, D. L. Rogow, J. A. Mason, T. M. McDonald, E. D. Bloch, Z. R. Herm, T. H. Bae and J. R. Long, *Chem. Rev.,* 2012, **112**, 724-781.

3. L. J. Murray, M. Dincă and J. R. Long, *Chem. Soc. Rev.,* 2009, **38**, 1294-1314.

4. J. Lee, O. K. Farha, J. Roberts, K. A. Scheidt, S. T. Nguyen and J. T. Hupp, *Chem. Soc. Rev.,* 2009, **38**, 1450-1459.

5. A. Corma, H. García and F. Llabrés i Xamena, *Chem. Rev.,* 2010, **110**, 4606-4655.

6. L. E. Kreno, K. Leong, O. K. Farha, M. Allendorf, R. P. Van Duyne and J. T. Hupp, *Chem. Rev.,* 2012, **112**, 1105-1125.

7. Y. Xu, Q. Li, H. Xue and H. Pang, *Coord. Chem. Rev,* 2018, **376**, 292-318.

8. S. Sundriyal, H. Kaur, S. K. Bhardwaj, S. Mishra, K.-H. Kim and A. Deep, *Coord. Chem. Rev,* 2018, **369**, 15-38.

9. A. Morozan and F. Jaouen, *Energy Environ. Sci.,* 2012, **5**, 9269-9290.

10. X.-W. Liu, T.-J. Sun, J.-L. Hu and S.-D. Wang, *J. Mater. Chem. A,* 2016, **4**, 3584-3616.

11. O. K. Farha, I. Eryazici, N. C. Jeong, B. G. Hauser, C. E. Wilmer, A. A. Sarjeant, R. Q. Snurr, S. T. Nguyen, A. O. Yazaydin and J. T. Hupp, *J. Am. Chem. Soc.,* 2012, **134**, 15016-15021.

12. M. Sevilla and R. Mokaya, *Energy Environ. Sci.,* 2014, **7**, 1250-1280.

13. P. Simon and Y. Gogotsi, *Nat. Mater.,* 2008, **7**, 845-854.

14. H. Ji, X. Zhao, Z. Qiao, J. Jung, Y. Zhu, Y. Lu, L. L. Zhang, A. H. MacDonald and R. S. Ruoff, *Nat. Commun.,*2014, **5**, 3317-3323.

15. Y. Xu, Z. Lin, X. Zhong, X. Huang, N. O. Weiss, Y. Huang and X. Duan, *Nat. Commun.,*2014, **5**, 4554-4562.

16. Y. Zhu, S. Murali, M. D. Stoller, K. J. Ganesh, W. Cai, P. J. Ferreira, A. Pirkle, R. M. Wallace, K. A. Cychosz, M. Thommes, D. Su, E. A. Stach and R. S. Ruoff, *Science,* 2011, **332**, 1537-1541.

17. J. Chmiola, G. Yushin, Y. Gogotsi, C. Portet, P. Simon and P.-L. Taberna, *Science,* 2006, **313**, 1760-1763.

18. T. Lin, I.-W. Chen, F. Liu, C. Yang, H. Bi, F. Xu and F. Huang, *Science,* 2015, **350**, 1508-1513.

19. M. Zhi, C. Xiang, J. Li, M. Li and N. Wu, *Nanoscale*, 2013, **5**, 72-88.

20. V. Augustyn, P. Simon and B. Dunn, *Energy Environ. Sci.* 2014, **7**, 1597-1614.

21. L. Shen, J. Wang, G. Xu, H. Li, H. Dou and X. Zhang, *Adv. Energy Mater.,* 2015, **5**, 1400977.

22. R. R. Salunkhe, J. Tang, Y. Kamachi, T. Nakato, J. H. Kim and Y. Yamauchi, *ACS Nano,* 2015, **9**, 6288-6296.

23. N. P. Wickramaratne, J. Xu, M. Wang, L. Zhu, L. Dai and M. Jaroniec, *Chem. Mater.,* 2014, **26**, 2820-2828.

24. F. Zhang, T. Liu, M. Li, M. Yu, Y. Luo, Y. Tong and Y. Li, *Nano Lett.,* 2017, **17**, 3097-3104.

25. L. Yao, Q. Wu, P. Zhang, J. Zhang, D. Wang, Y. Li, X. Ren, H. Mi, L. Deng and Z. Zheng, *Adv. Mater.,* 2018, **30**, 1706054.

26. A. Vu, X. Li, J. Phillips, A. Han, W. H. Smyrl, P. Bühlmann and A. Stein, *Chem. Mater.*, 2013, **25**, 4137-4148.

27. H. M. Jeong, J. W. Lee, W. H. Shin, Y. J. Choi, H. J. Shin, J. K. Kang and J. W. Choi,

Journal of Materials Chemistry A Accepted Manuscript

Nano Lett., 2011, **11**, 2472-2477.

28.   L. L. Zhang, X. Zhao, H. Ji, M. D. Stoller, L. Lai, S. Murali, S. McDonnell, B. Cleveger, R. M. Wallace and R. S. Ruoff, *Energy Environ. Sci.,* 2012, **5**, 9618-9625.

29.   W. Xia, A. Mahmood, R. Zou and Q. Xu, *Energy Environ. Sci.,* 2015, **8**, 1837-1866.

30.   B. Liu, H. Shioyama, T. Akita and Q. Xu, *J. Am. Chem. Soc.,* 2008, **130**, 5390-5391.

31.   J.-K. Sun and Q. Xu, *Energy Environ. Sci.,* 2014, **7**, 2071-2100.

32.   H. L. Jiang, B. Liu, Y. Q. Lan, K. Kuratani, T. Akita, H. Shioyama, F. Zong and Q. Xu, *J. Am. Chem. Soc.* 2011, **133**, 11854-11857.

33.   P. Pachfule, D. Shinde, M. Majumder and Q. Xu, *Nat. Chem.,* 2016, **8**, 718-724.

34.   J. Hu, H. Wang, Q. Gao and H. Guo, *Carbon*, 2010, **48**, 3599-3606.

35.   J. Wang, X. Luo, C. Young, J. Kim, Y. V. Kaneti, J. You, Y.-M. Kang, Y. Yamauchi and K. C. W. Wu, *Chem. Mater.,* 2018, **30**, 4401-4408.

36.   W. Chaikittisilp, M. Hu, H. Wang, H. S. Huang, T. Fujita, K. C. Wu, L. C. Chen, Y. Yamauchi and K. Ariga, *Chem. Commun.,* 2012, **48**, 7259-7261.

37.   M. G. Campbell, D. Sheberla, S. F. Liu, T. M. Swager and M. Dincă, *Angew. Chem., Int. Ed.,* 2015, **54**, 4349-4352.

38.   L. Sun, M. G. Campbell and M. Dincă, *Angew. Chem., Int. Ed.,* 2016, **55**, 3566-3579.

39.   D. Sheberla, L. Sun, M. A. Blood-Forsythe, S. Er, C. R. Wade, C. K. Brozek, A. Aspuru-Guzik and M. Dincă, *J. Am. Chem. Soc.,* 2014, **136**, 8859-8862.

40.   R. Dong, P. Han, H. Arora, M. Ballabio, M. Karakus, Z. Zhang, C. Shekhar, P. Adler, P. S. Petkov, A. Erbe, S. C. B. Mannsfeld, C. Felser, T. Heine, M. Bonn, X. Feng and E. Canovas, *Nat. Mater.,* 2018, **17**, 1027-1032.

41.   D. Sheberla, J. C. Bachman, J. S. Elias, C. J. Sun, Y. Shao-Horn and M. Dincă, *Nat. Mater.,* 2017, **16**, 220-224.

42.   W. H. Li, K. Ding, H. R. Tian, M. S. Yao, B. Nath, W. H. Deng, Y. Wang and G. Xu, *Adv. Funct. Mater.,* 2017, **27**, 1702067.

43.   X. Xu, J. Tang, H. Qian, S. Hou, Y. Bando, M. S. A. Hossain, L. Pan and Y. Yamauchi, *ACS Appl. Mater. Interfaces,* 2017, **9**, 38737-38744.

44.   D. Fu, H. Zhou, X.-M. Zhang, G. Han, Y. Chang and H. Li, *ChemistrySelect,* 2016, **1**, 285-289.

45.   Y. Zhang, B. Lin, Y. Sun, X. Zhang, H. Yang and J. Wang, *RSC Adv.,* 2015, **5**, 58100-

58106.

46.   K. M. Choi, H. M. Jeong, J. H. Park, Y.-B. Zhang, J. K. Kang and O. M. Yaghi, *ACS Nano,* 2014, **8**, 7451-7457.

47.   L. Wang, X. Feng, L. Ren, Q. Piao, J. Zhong, Y. Wang, H. Li, Y. Chen and B. Wang, *J. Am. Chem. Soc.,* 2015, **137**, 4920-4923.

48.   P. Srimuk, S. Luanwuthi, A. Krittayavathananon and M. Sawangphruk, *Electrochimica. Acta,* 2015, **157**, 69-77.

49.   M. Sindoro, N. Yanai, A.-Y. Jee and S. Granick, *Acc. Chem. Res.,* 2013, **47**, 459-469.

50.   X. Fan, C. Yu, J. Yang, Z. Ling, C. Hu, M. Zhang, J. Qiu, *Adv. Energy Mater.,* 2015, **5**, 1401761.

51.   S. Dong, X. He, H. Zhang, X. Xie, M. Yu, C. Yu, N. Xiao, J. Qiu, *J. Mater. Chem. A,* 2018, **6**, 15954-15960.

52.   X. He, X. Li, H. Ma, J. Han, H. Zhang, C. Yu, N. Xiao, J. Qiu, J. Power Sources, 2017, **340**, 183-191.

53.   A. Stein, B. E. Wilson, S. G. Rudisill, *Chem. Soc. Rev.,* 2013, **42**, 2763-2803.

54.   W. C. Yoo, S. Kumar, R. L. Penn, M. Tsapatsis and A. Stein, *J. Am. Chem. Soc.,* 2009, **131**, 12377-12383.

55.   W. Fan, M. A. Snyder, S. Kumar, P.-S. Lee, W. C. Yoo, A. V. McCormick, R. L. Penn, A. Stein, M. Tsapatsis, *Nat. Mater.,* 2008, **7**, 984-991.

56.   P. Pachfule, B. K. Balan, S. Kurungot and R. Banerjee, *Chem. Commun.,* 2012, **48,** 2009-2011.

57.   A. Sachse, R. Ameloot, B. Coq, F. Fajula, B. Coasne, D. De Vos and A. Galarneau, *Chem. Commun.,* 2012, **48**, 4749-4751.

58.   C. A. de Oliveira, F. F. da Silva, G. C. Jimenez, J. F. Neto, D. M. de Souza, I. A. de Souza and S. Alves, Jr., *Chem. Commun.,* 2013, **49**, 6486-6488.

59.   Y. Zhang, X. Bo, C. Luhana, H. Wang, M. Li and L. Guo, *Chem. Commun.,* 2013, **49**, 6885-6887.

60.   I. Luz, M. Soukri and M. Lail, *Chem. Mater.,* 2017, **29**, 9628-9638.

61.   L. Dai, Y. Xue, L. Qu, H. J. Choi and J. B. Baek, *Chem. Rev.,* 2015, **115**, 4823-4892.

62.   Z. Pei, H. Li, Y. Huang, Q. Xue, Y. Huang, M. Zhu, Z. Wang and C. Zhi, *Energy Environ. Sci,* 2017, **10**, 742-749.

63.   K. Gong, F. Du, Z. Xia, M. Durstock and L. Dai, *Science,* 2009, **323**, 760-764.

26

64.   H. W. Liang, W. Wei, Z. S. Wu, X. Feng and K. Mullen, *J. Am. Chem. Soc.*, 2013, **135**, 16002-16005.

65.   M. Lefèvre, E. Proietti, F. Jaouen and J.-P. Dodelet, *Science,* 2009, **324**, 71-74.

66.   H. S. Kim, M. Kim, M. S. Kang, J. Ahn, Y.-E. Sung and W. C. Yoo, *ACS Sustainable Chem. Eng.,* 2017, **6**, 2324-2333.

67.   M. Shao, Q. Chang, J. P. Dodelet and R. Chenitz, *Chem. Rev.,* 2016, **116**, 3594-3657.

68.   E. M. Miner, T. Fukushima, D. Sheberla, L. Sun, Y. Surendranath and M. Dincă, *Nat. Commun.,* 2016, **7**, 10942-10949.

69.   M. Jahan, Q. Bao and K. P. Loh, *J. Am. Chem. Soc.,* 2012, **134**, 6707-6713.

70.   M. Jahan, Z. Liu and K. P. Loh, *Adv. Funct. Mater.,* 2013, **23**, 5363-5372.

71.   M. Sánchez-Sánchez, N. Getachew, K. Díaz, M. Díaz-García, Y. Chebude and I. Díaz, *Green Chem.,* 2015, **17**, 1500-1509.

72.   W. C. Yoo, S. Kumar, Z. Wang, N. S. Ergang, W. Fan, G. N. Karanikolos, A. V. McCormick, R. L. Penn, M. Tsapatsis and A. Stein, *Angew. Chem., Int. Ed.,* 2008, **47**, 9096-9099.

73.   C. R. Wade and M. Dincă, *Dalton Trans.,* 2012, **41**, 7931-7938.

74.   B. Vidhyadharan, I. I. Misnon, R. A. Aziz, K. P. Padmasree, M. M. Yusoff and R. Jose, *J. Mater. Chem. A,* 2014, **2**, 6578-6588.

75.   C. Wang, J. Xu, M.-F. Yuen, J. Zhang, Y. Li, X. Chen and W. Zhang, *Adv. Funct. Mater.,*   2014, **24**, 6372-6380.

76.   Z. Li, J. Liu, K. Jiang and T. Thundat, *Nano Energy.* 2016, **25**, 161-169.

77.   Y. Nie, L. Li and Z. Wei, *Chem. Soc. Rev.* 2015, **44**, 2168-2201.

78.   M. Kim, H. S. Kim, S. J. Yoo, W. C. Yoo and Y.-E. Sung, *J. Mater. Chem. A,* 2017, **5**, 4199-4206.

79.   K. Mayrhofer, D. Strmcnik, B. Blizanac, V. Stamenkovic, M. Arenz and N. Markovic, *Electrochim. Acta,* 2008, **53**, 3181-3188
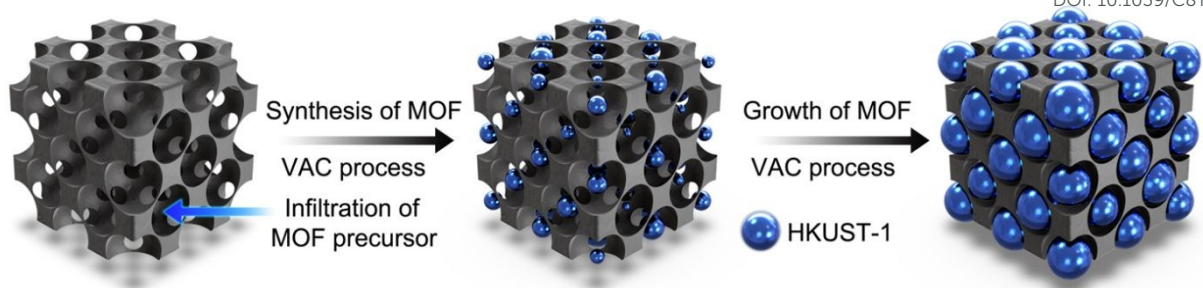
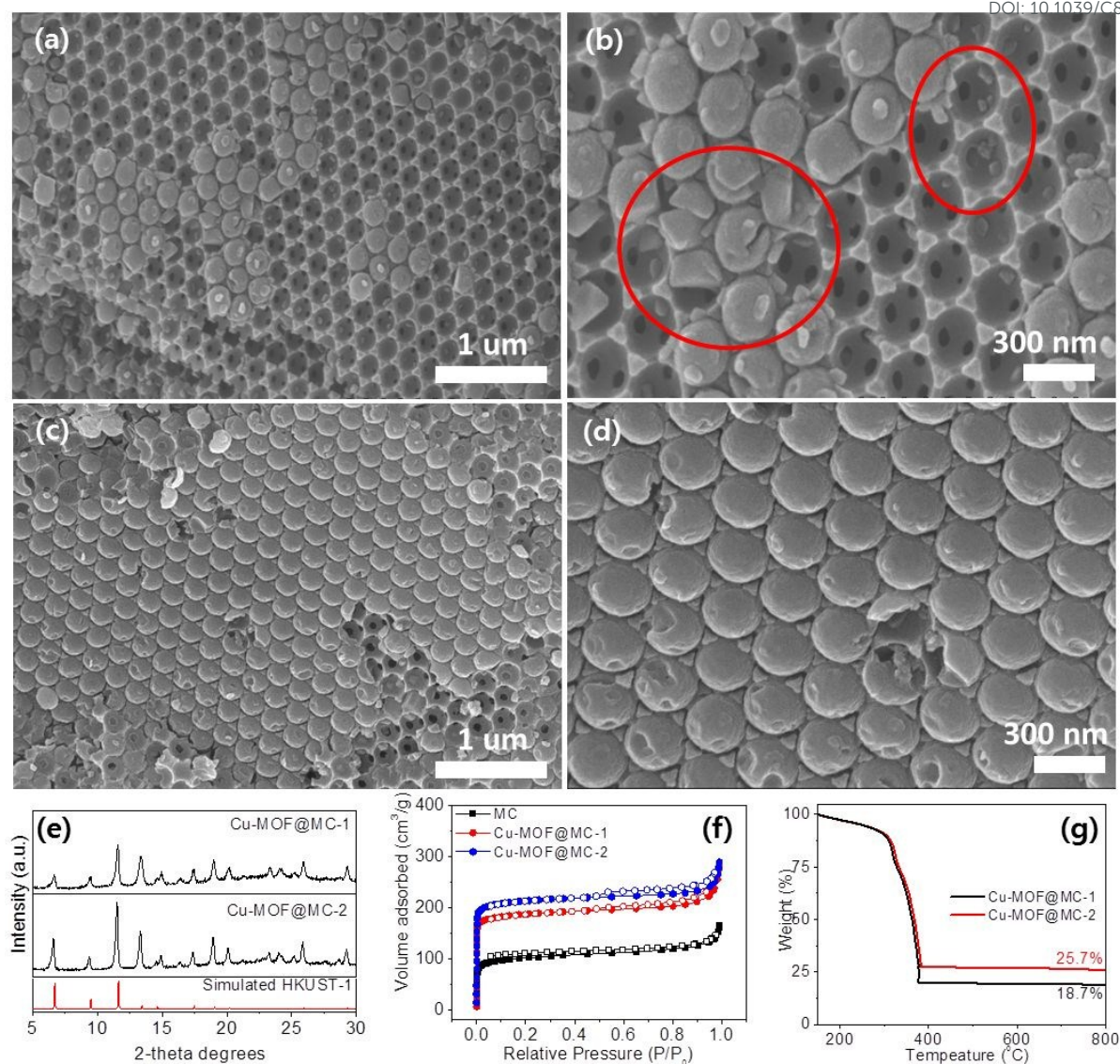**Scheme 1.** Synthetic scheme of MOF@CM via VAC process.

Figure 1. Characterization of Cu-MOF@MC sample synthesized by the sequential VAC processes: low magnification SEM images (a and c) and enlarged SEM images (b and d) of Cu-MOF@MC-1 and Cu-MOF@MC-2, respectively, and XRD (e), N_2 sorption isotherms (f), and TGA profiles (g) of Cu-MOF@MC samples.
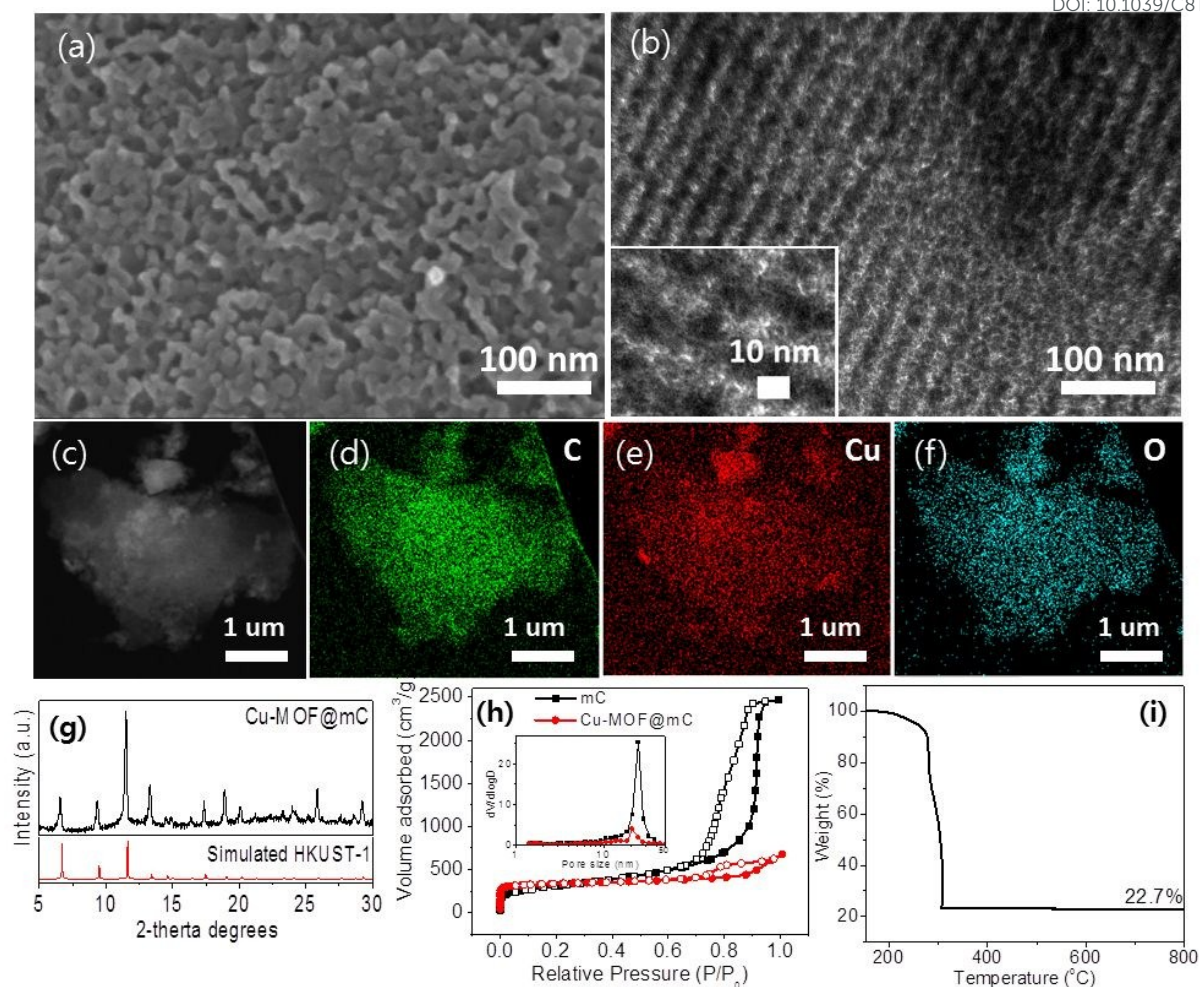
29

Journal of Materials Chemistry A

Figure 2. Characterization of Cu-MOF@mC: SEM image (a) and TEM (b) image with high magnification image as an inset, HAADF-STEM image (c) with elementary mapping of the corresponding images of C (d), Cu (e), and O (f), and XRD data (g), N_2 sorption isotherms (h), and TGA result (i) of Cu-MOF@mC.
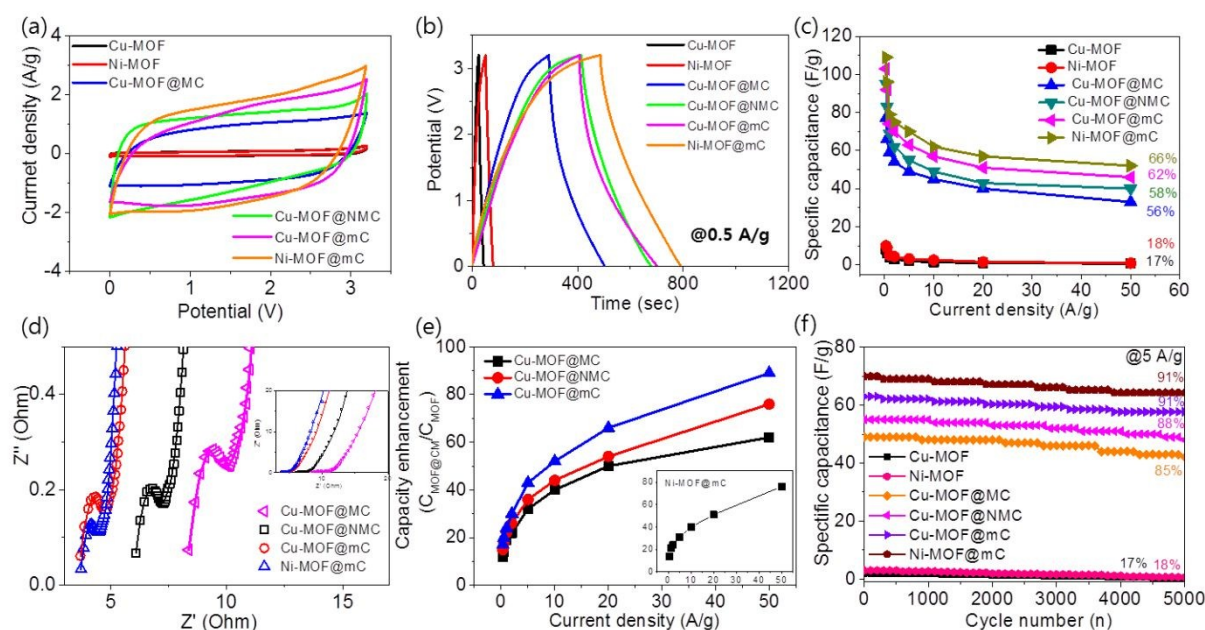
Figure 3. Electrochemical properties of the pristine MOFs and MOF@CM samples: comparison of CV curves (a) measured at scan rate of 200 mV/s, charge-discharge profiles (b) at current density of 0.5 A/g, and capacitance retentions (c) at various current densities for the pristine MOFs and MOF@CM samples, and the Nyquist plot (d) in a high frequency range with inset of full range of the Nyquist plots for MOF@CMs, capacity enhancement profiles (e) at various current densities obtained from the ratio of boosted capacitances of Cu-MOFs incorporated within conductive CMs and capacitance of the pristine Cu-MOF (inset for capacity enhancement for Ni-MOF@mC), and long-term stability profiles (f) at current density of 5 A/g for 5000 cycles for the pristine MOFs and MOF@CMs.
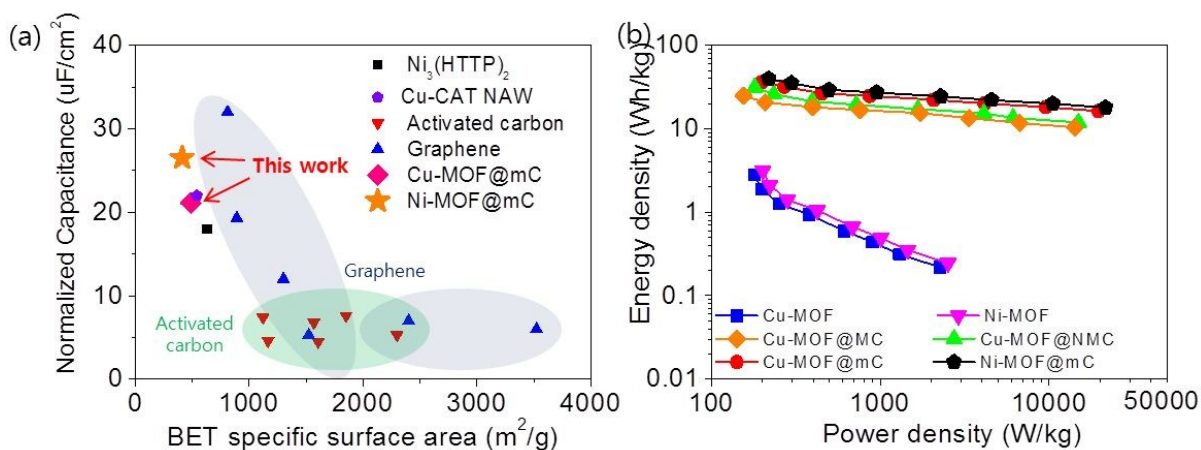
Figure 4. Comparison of the SSA normalized capacitances for Cu-/Ni-MOF@mCs and various EDLCs listed in the Table S4 (a) and Ragone plots of the pristine MOFs and MOF@CMs (b).
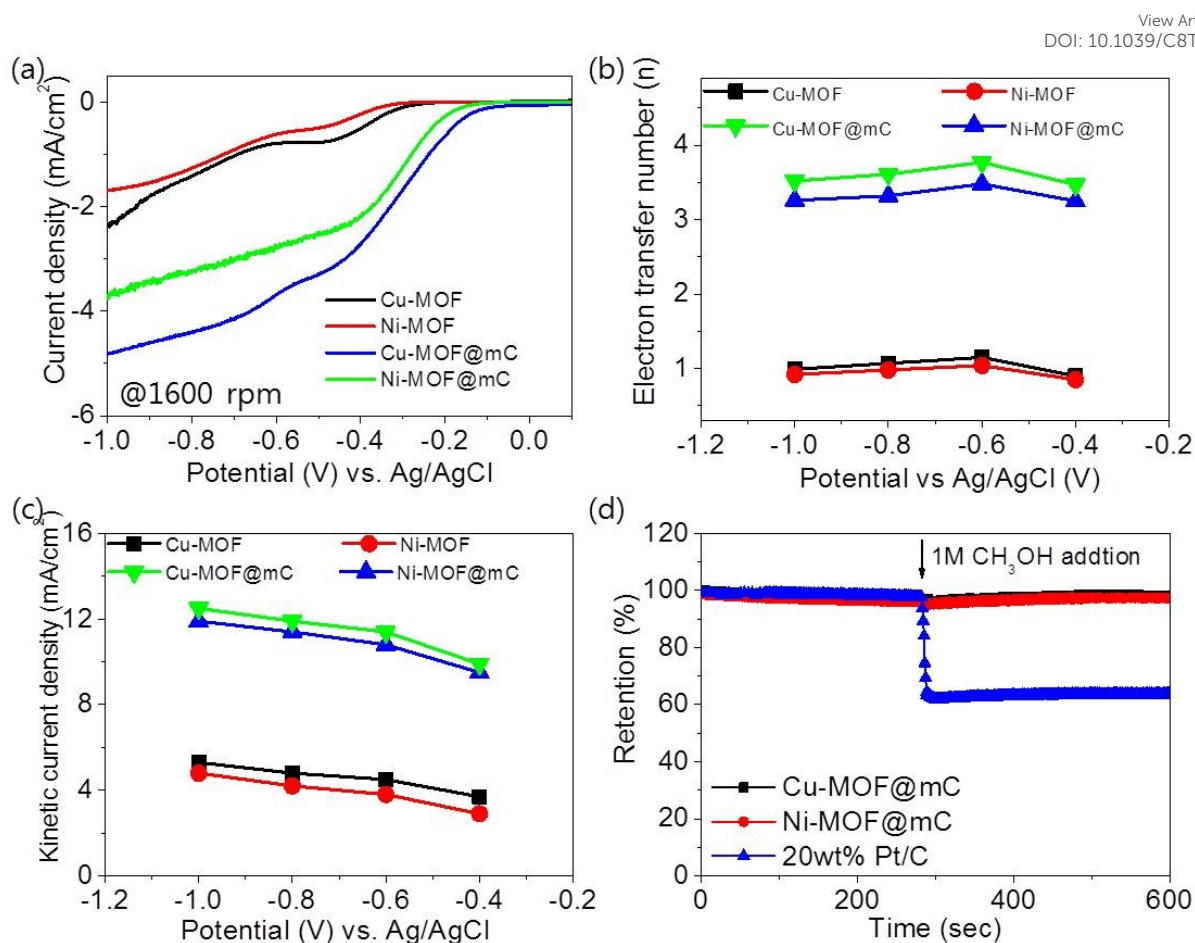
Figure 5. RDE polarization curves obtained at 1600 rpm in O_2-saturated 0.1 M KOH (a), electron transfer numbers derived from KL plots at various potentials vs. Ag/AgCl (b), kinetic current densities at various potentials vs. Ag/AgCl (c) of the pristine MOFs and Cu-/Ni-MOF@mCs, and chronoamperometric responses at -0.4 V vs. Ag/AgCl of 20 wt% Pt/C and Cu-/Ni-MOF@mCs (d).

Table 1. Textural properties of the pristine MOFs and MOF@CM samples, and volume fractions of MOF inside various CMs.

Sample	V_{micro} (cc/g)[a]	V_{tot} (cc/g)[b]	S_{BET} (m^2/g)	TGA (wt%)[c]	Volume fraction of MOF inside CM (%) (micropore volume /TGA)[d]
Cu-MOF	0.49	0.55	1146		-
Ni-MOF	0.30	0.32	561		-
MC	0.15	0.25	391		-
NMC	0.11	0.18	302		-
mC	0.04	4.0	1107		-
Cu-MOF@MC-1	0.28	0.42	743	18.7	64 /57
Cu-MOF@MC	0.33	0.44	848	25.7	76 /78
Cu-MOF@NMC	0.32	0.41	808	24.7	75 /75
Cu-MOF@mC	0.28	0.92	488	22.7	68 /69
Ni-MOF@mC	0.17	0.55	411	18.5	67 /59

[a]Obtained from the *t*-plot method; [b]Measured at P/P0 = 0.99; [c]Leftover weight percentage of TGA measurement performed under air condition; [d]Calculation from micropore volume and TGA data of MOF@CM samples (see the note 1 in the supporting information for the detail calculation)

Journal of Materials Chemistry A Accepted Manuscript